Results in Engineering 5 (2020) 100074

Contents lists available at ScienceDirect

Results in Engineering

journal homepage: www.editorialmanager.com/rineng/Default.aspx

Allowable solar flux densities for molten-salt receivers: Input to the aiming strategy

Alberto Sánchez-González *, María Reyes Rodríguez-Sánchez, Domingo Santana

Energy Systems Engineering Group (ISE), Department of Thermal and Fluid Engineering, Universidad Carlos III de Madrid, Av. Universidad, 30, 28911, Leganés, Madrid, Spain

ARTICLE INFO

Keywords:
Solar power tower
Molten-salt corrosion
Thermal stress
Tube alloy and geometry
Heliostat field aiming strategy

ABSTRACT

Solar Power Tower technology requires accurate models and tools to assist in design and operation stages. The heliostat field aiming strategy seeks the maximization of the thermal output from the receiver, while preventing its permanent damage because of thermal stress and corrosion in molten salt receivers. These two limitations are translated into Allowable Flux Densities (AFD), which can be handled by the aiming strategy.

This paper explains the methodology to determine AFDs, and analyzes the influence of tube geometry and material. AFD by corrosion is slightly lower in Haynes 230 than Inconel 625 and austenitic alloys. On the contrary, HA230 has better performance than In625 under thermal stress. Increment of tube wall thickness diminishes the AFD: slightly by corrosion, but significantly by thermal stress.

The generated AFD databases feed the aiming model, herein applied to Gemasolar case study. In the cylindrical receiver, first northern panels are limited by thermal stress, while the last ones by corrosion. Under optimized aiming, HA230 receiver tubes produce equivalent thermal output than In625.

1. Introduction

Deployment and consolidation of Solar Power Tower (SPT) technology demand the development of accurate tools to assist in design and operation phases. In the operation of central receivers working with molten-salt as heat transfer fluid, corrosion and thermal stress are the most critical issues, which may cause permanent damage.

Central molten-salt receivers consist of panels made up of tubes connected in parallel. Material and size of the receiver tubes have a great influence on the maximum incident flux of concentrated solar radiation that they can withstand safely. Nickel-based alloys with around 15–20% chromium content perform best in contact with high temperature molten-salt [1]. This is why stainless steel of grade 321 (17.3% Cr), 347 (17.5%), Inconel 625 (21.8%) and Haynes 230 (22.4%) are commonly utilized, mainly the last two, in the construction of molten-salt receivers.

The concept of Allowable Flux Density (AFD) was originally introduced by Vant-Hull [2] as the maximum incident flux density to safely operate the receiver. For Solar Two receiver, he presented two correlations to relate thermal stress and corrosion with AFD, which are dependent on salt temperature and velocity. Later studies further explored the AFD limits due to thermal stress in molten-salt [3] and steam [4] receivers.

The authors developed an aiming strategy model [5] that is fed by a database of precalculated AFDs. This model accommodates the aim points of all the heliostats in the field, so that the incident flux on the receiver matches (or not exceeds) the AFD limit at any point.

Other researchers working on aiming strategies have recently adopted the AFD approach in their developments, as in Refs. [6,7].

The goal of this paper is to provide further insight on the determination of AFD for molten-salt receivers. The methodologies to translate corrosion and thermal stress constraints into AFD are respectively described in Sections 2 and 3. The results in these Sections show the effect of tube material and geometry (diameter and thickness) on the AFD by both corrosion and stress. For Gemasolar case study, Section 4 applies the generated AFD databases to the aiming strategy model.

2. Corrosion limit

Nitrate molten-salt (60% $NaNO_3$ and 40% KNO_3) at high temperatures becomes corrosive to metallic tubes. This Section explains the methodology to determine the allowable flux densities by corrosion (AFD_{corr}), providing also results for selected alloys and tube geometries.

Kruizenga et al. [8] studied the corrosion rates in four alloys of interest immersed in molten-salt: iron-based 321SS and 347SS, and nickel-based Inconel 625 (In625) and Haynes 230 (HA230). The metal

* Corresponding author.
E-mail address: asgonzal@ing.uc3m.es (A. Sánchez-González).

https://doi.org/10.1016/j.rineng.2019.100074
Received 10 September 2019; Received in revised form 15 November 2019; Accepted 20 November 2019

Nomenclature

d	Tube diameter [mm]
E	Young's modulus [GPa]
F	Flux density [W/m^2]
f_{sp}	Spillage loss factor [−]
k	Aiming factor [−]
$\dot{m}_{s,t}$	Mass flow rate of salt throughout a tube [kg/s]
q	Heat flux density by conduction [W/m^2]
Q_{rec}	Heat power intercepted by receiver [MW]
R^2	Coefficient of correlation
T	Temperature [ºC]
t	Tube thickness [mm]
UTS	Ultimate tensile strength [MPa]
x	Horizontal coordinate along panel width [m]
z	Vertical coordinate along flowpath [m]

Greek symbols

γ	Coefficient of thermal expansion [mm/m·K]
κ	Thermal conductivity [W/m·K]
ν	Poisson's ratio [−]
σ	Thermal stress [MPa]

Subscripts

c	tube crown
corr	corrosion
E	East flowpath
f	film
i	inner
lim	limit
o	outer
s	salt
strs	thermal stress
w	wall
W	West flowpath

Acronyms

321SS	Stainless Steel grade 321
347SS	Stainless Steel grade 347
AFD	Allowable Flux Density [W/m^2]
HA230	Haynes 230 alloy
In625	Inconel alloy 625
SPT	Solar Power Tower

loss rates in μm/year at 400, 500, 600 and 680 °C salt temperatures (T_s) are reported in Fig. 1; solid curves represent the power fitting on the experimental data ($R^2 = 1$).

As can be seen in Fig. 1, corrosion triggers at around 600 °C. To limit corrosion damage, maximum salt temperature for each alloy is found out on the basis of a common criterion. Acceptable maximum metal loss rate is established in 50 μm/year; which implies a maximum loss of 0.5 mm in tube thickness for 10 years. As a result, the limiting temperatures are 628 °C for In625, 620 °C for HA230, 626 °C for 321SS and 632 °C for 347SS (Fig. 1). The maximum salt temperature within irradiated receiver tubes takes place in contact with the inner tube surface, therefore those values are labeled as the limiting film temperatures by corrosion, $T_{f,lim}$.

These limiting film temperatures are reached at specific incident flux densities that can be computed *a priori*. Given a tube geometry, the resulting allowable flux density by corrosion ultimately depends on molten-salt bulk temperature and mass flow rate; *i.e.* $\text{AFD}_{corr}(T_s, \dot{m}_{s,t})$. Fig. 2 represents the flowchart to generate databases of AFD_{corr}. This iterative procedure finds the flux density provoking a film temperature equal to $T_{f,lim}$ at each cross-section of a virtual tube, whose inlet and outlet temperatures are 290 and 565 °C, as usual in nitrate molten salt receivers. The outermost loop sweeps a sequence of $\dot{m}_{s,t}$, herein from 0.8 to 4.8 kg/s in increments of 0.4 kg/s.

The core of the calculation relies on the heat transfer model validated for molten-salt receivers [9]. This model discretizes a single representative tube per panel, and considers temperature variations in both axial and circumferential directions. In this model, the net radiation method deals with the heat flux absorbed by each tube cell, and the crossed-string method calculates the view factors [10]. Nitrate molten-salt properties are taken from Zavoico [11].

The resulting AFD_{corr} datasets are now presented for different metal alloys (In625, HA230, 321SS and 347SS) and tube geometries. As reference geometry is taken 25 mm in outer diameter (d_o), and 1.5 mm in wall thickness (t). Cases for thicker wall tube and greater cross-section are also summarized in Table 1.

Figs. 3–5 show for different alloys and tube geometries the allowable flux density by corrosion as a function of salt temperature (abscissa) and

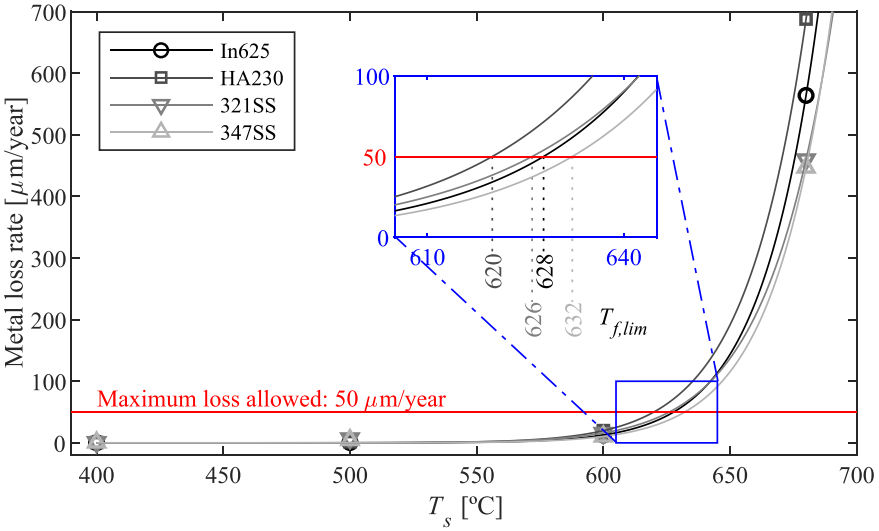

Fig. 1. Metal loss rates for selected metals, according to Ref. [8]. Limiting film temperatures based on loss of 50 μm/year.

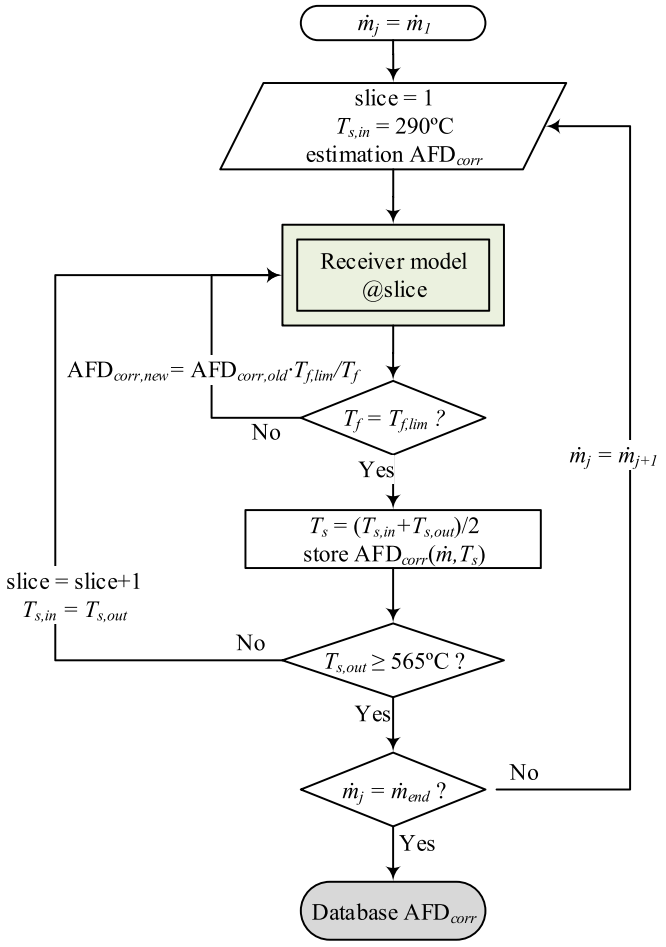

Fig. 2. Flowchart for the generation of the database of allowable flux densities by corrosion.

mass flow rate per tube (color lines). The behavior of AFD$_{corr}$ is regular: it decreases with mass flow rate, whilst it decreases when molten-salt temperature increases. Besides, the decrement of AFD$_{corr}$ is more pronounced at higher mass flow rates. This behavior is in agreement with the correlation equation proposed by Vant-Hull in Ref. [2].

Fig. 3 represents AFD$_{corr}$ for nickel-based alloys and reference tube geometry. Since the limiting film temperature of In625 is higher than that of HA230 (628 *vs* 620 °C), AFD$_{corr}$ is greater in In625 given the same T_s and $\dot{m}_{s,t}$.

Tube geometry has also influence on the AFD$_{corr}$ limits. For the wider In625 tube (outer diameter: 35 mm) in Fig. 4 (left), the AFD$_{corr}$ dramatically decreases respect to reference 25 mm tube (Fig. 3 (left)), taking the same $\dot{m}_{s,t}$. This is simply explained by the decrease of fluid velocity because of cross-section increment. Thicker 2 mm wall tube, keeping the 22 mm inner diameter for proper $\dot{m}_{s,t}$ comparison (Fig. 4 (right) *vs*. Fig. 3 (left)), slightly brings down the AFD$_{corr}$. The rise of tube thermal resistance with wall thickness explains this fact.

AFD$_{corr}$ databases for reference tubes of austenitic alloys (Fig. 5) follow the same pattern as for nickel alloys (Fig. 3). The values of film limit temperatures for each alloy justifies the following decreasing sequence of AFD$_{corr}$ (constant T_s and $\dot{m}_{s,t}$): 347SS > In625 > 321SS > HA230.

Table 1
Tube geometries.

Case	d_i [mm]	d_o [mm]	t [mm]
Reference	22	25	1.5
Thicker	22	26	2.0
Wider section	32	35	1.5

3. Thermal stress limit

Receiver tubes exposed to incident concentrated solar radiation leads to circumferential and radial temperature gradients in the tubes. The resulting thermal stress (σ), which is maximum at the tube front, or crown (denoted by subscript c), was estimated by Babcock & Wilcox [12] via Eq. (1). This equation, recently adopted by other authors such as [13, 14], results from the superposition of thermal stresses due to: circumferential gradient, as considered in the first term of Eq. (1); and radial gradient, second term of the equation.

$$\sigma_c = \gamma E\left[(\overline{T}_c - \overline{T}_w) + \frac{\Delta T_c}{2(1-\nu)}\right] \quad (1)$$

For a given tube section, the following three equations respectively estimate: radial temperature difference at the crown (ΔT_c), mean temperature at the crown ($\overline{T}_c$), and average tube temperature ($\overline{T}_w$). The latter expression, Eq. (4), results from the integration of the tube temperature considering a cosine distribution from the crown at $\overline{T}_c$ to the back of the tube at temperature equal to that of the salt (T_s). In Eqs. (2) and (3), $T_{w,c}$ stands for the outer tube temperature at the crown.

$$\Delta T_c = T_{w,c} - T_f \quad (2)$$

$$\overline{T}_c = \frac{T_{w,c} + T_f}{2} \quad (3)$$

$$\overline{T}_w = T_s + \frac{1}{\pi}(\overline{T}_c - T_s) \quad (4)$$

The mechanical properties, referred to in Babcock & Wilcox's Eq. (1), depend on the wall temperature of the tube (T_w). For the selected alloys, those properties can be found in ASME's Boiler and Pressure Vessel Code [15]. Fig. 6 (right) represents Young's modulus (E) and Fig. 7 (left) the coefficient of thermal expansion (γ). Poisson's ratio (ν) is 0.31 for all four selected alloys. As we are interested in finding out the thermal stress limits, rather than generic stresses (σ_c in Eq. (1)), the ultimate tensile strength (*UTS*) will be employed. *UTS* as a function of tube wall temperature is shown in Fig. 6 (left).

On the other hand, from conduction heat transfer it is well known the heat flux density in a tube subjected to a radial temperature difference. At tube crown and on its outer surface, the conductive heat flux density follows Eq. (5), where ΔT_c is as defined in Eq. (2) and κ stands for the thermal conductivity. Fig. 7 (right) shows κ as a function of wall temperature for the selected alloys, as retrieved from ASME Code [15].

$$q_c = \frac{2 \cdot \kappa \cdot \Delta T_c}{d_o \cdot \ln(d_o/d_i)} \quad (5)$$

In order to find out the thermal stress limit in terms of heat flux density, Eqs. (1) and (5) must be combined, using *UTS* in the former one. For the sake of convenience, film temperature T_f (considered equal to the inner tube wall temperature) can be eliminated from Eq. (1), resulting into Eq. (6). In this way, the stress correlation is only dependent on the $T_{w,c}$ (as mechanical properties) and salt bulk temperature.

$$UTS = \gamma E\left[\Delta T_c\left(\frac{1}{2(1-\nu)} + \frac{1-\pi}{2\pi}\right) + (T_{w,c} - T_s)\frac{\pi - 1}{\pi}\right] \quad (6)$$

In the combination of now Eqs. (5) and (6), the temperature difference at the crown (ΔT_c) is eliminated yielding to Eq. (7). This expression serves to the calculation in W/m^2 of the limiting heat flux density by conduction at the tube crown ($q_{lim,strs}$), which is just a function of wall and salt temperatures.

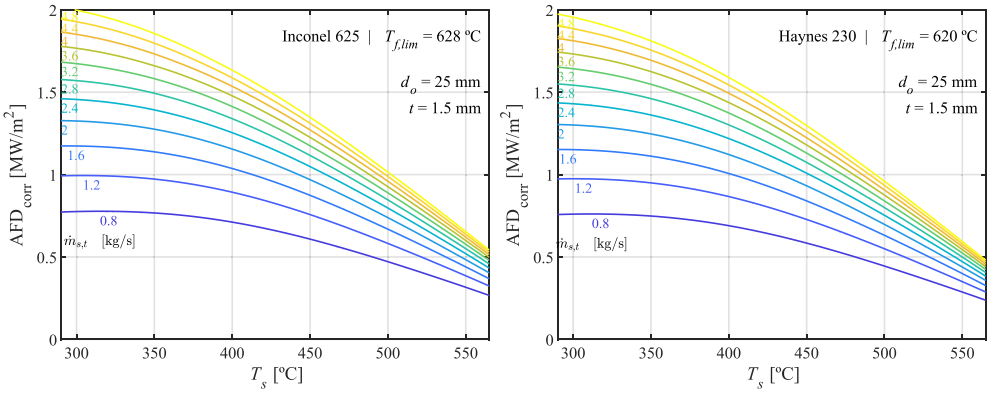

Fig. 3. Allowable flux densities by corrosion for tubes of In625 (left) and HA230 (right).

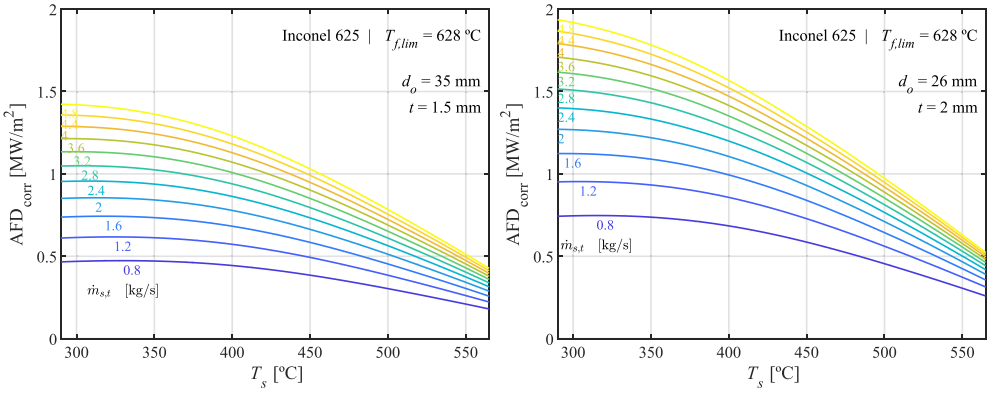

Fig. 4. Allowable flux densities by corrosion for In625 tube with another diameter (left) and thickness (right).

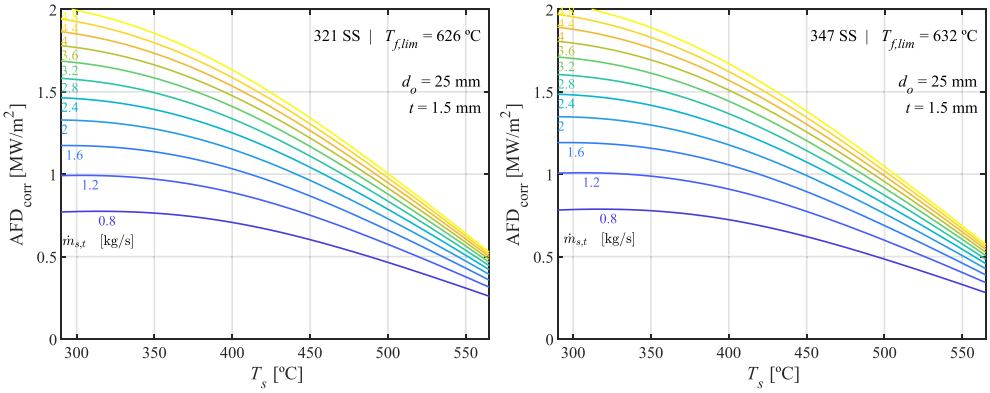

Fig. 5. Allowable flux densities by corrosion for tubes of 321SS (left) and 347SS (right).

$$q_{\lim,strs} = \frac{4 \cdot \kappa \cdot \left[\frac{UTS}{\gamma E} + (T_{w,c} - T_s)\frac{1-\pi}{\pi}\right]}{d_o \cdot \ln(d_o/d_i) \cdot \left[\frac{1}{1-\nu} + \frac{1-\pi}{\pi}\right]} \tag{7}$$

Because of convection and radiation losses to the surroundings, the limit of thermal stress in terms of incident flux density limit ($F_{lim,strs}$) is actually higher to the output from Eq. (7). Those losses are added to $q_{lim,strs}$ by means of Siebers & Kraabel convection correlation [16] and Stefan-Boltzmann radiation law at the crown; finally obtaining $F_{lim,strs}$.

Figs. 8 and 9 represent the flux density limit by stress depending on salt (in abscissa) and wall (color scale) temperatures. In general, it can be said that $F_{lim,strs}$ increases with increasing T_s, but with decreasing T_w.

Given Inconel 625 tubes of 25 mm in outer diameter, Fig. 8 depicts such stress limit whether the wall thickness is 1.5 mm (left) or 2.0 mm (right). It is clear from the chart that, for the same T_s and T_w, the smaller the tube thickness, the higher the flux limit by stress is. As $\ln(d_o/d_i)$ is in the denominator of Eq. (7), this explains why thinner wall tubes have higher allowance by thermal stress. The effect of tube diameter on the stress limit is almost negligible compared to that of the wall thickness.

Given a tube wall thickness of 1.5 mm, Fig. 9 shows the resulting $F_{lim,strs}$ for Haynes 230 (left) and 321SS (right). Compared to In625, HA230 has slightly higher limit, but 321SS limit is noticeable smaller than both of them. 347SS has smaller *UTS* than 321SS, leading to lower flux limits for 347SS as the rest of the mechanical properties are the same for both austenitic alloys.

Strictly speaking, the $F_{lim,strs}$ obtained until this point is not equivalent to the allowable flux density by thermal stress (AFD$_{strs}$). Such AFD$_{strs}$ is

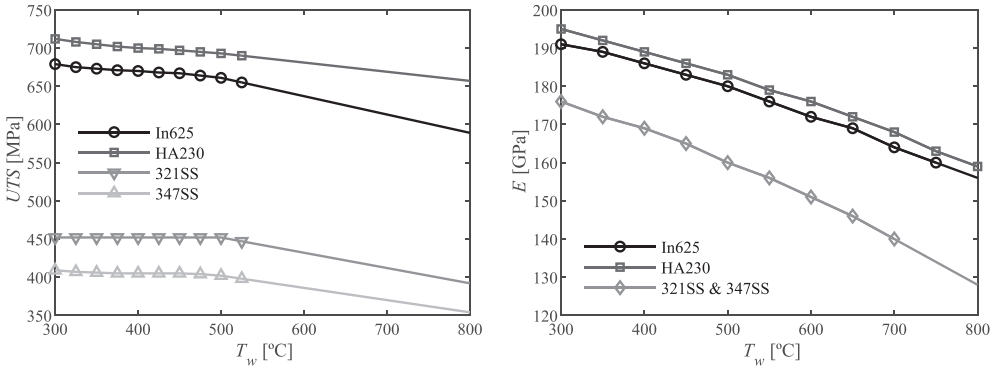

Fig. 6. Mechanical properties of tubes of selected materials: ultimate tensile strength (left) and Young's modulus (right).

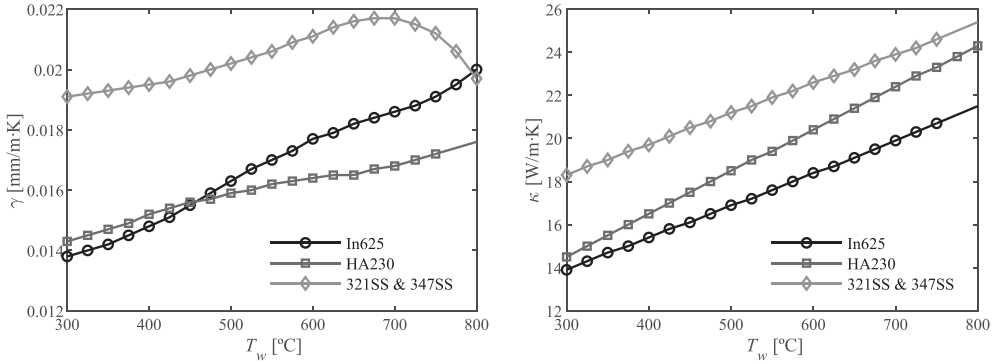

Fig. 7. Thermal properties of tubes of selected materials: thermal expansion (left) and conductivity (right).

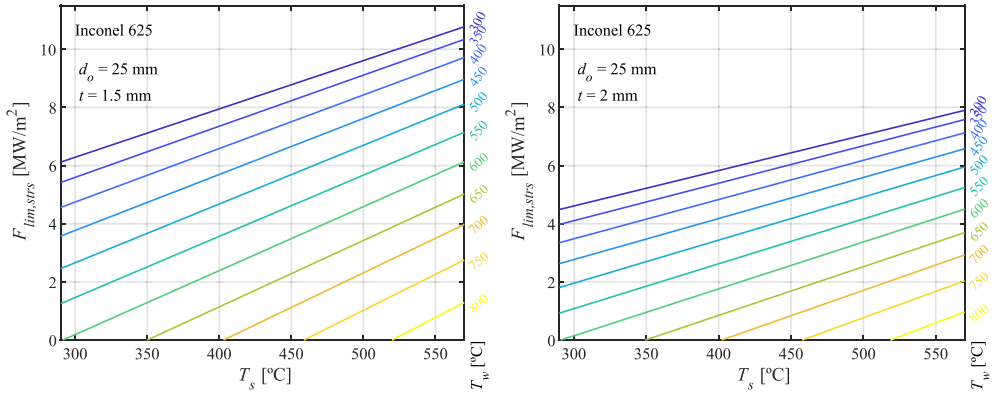

Fig. 8. Limits of flux density by thermal stress for In625 tube of thickness 1.5 (left) and 2.0 mm (right).

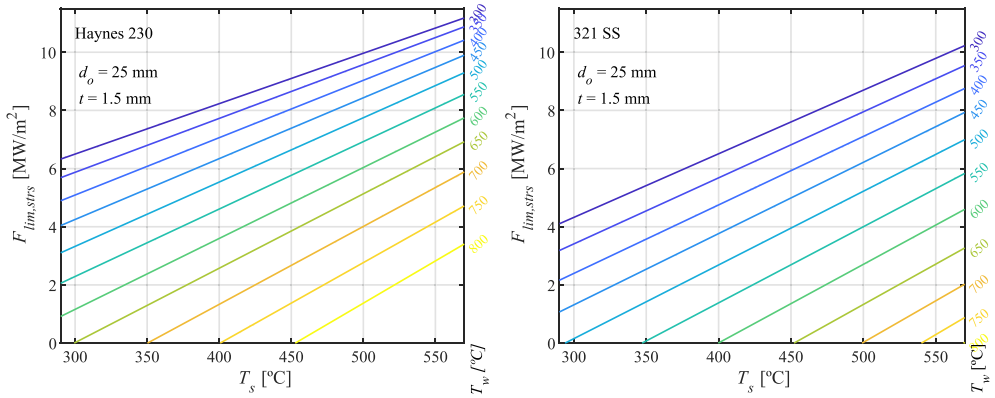

Fig. 9. Limits of flux density by thermal stress for tubes of HA230 (left) and 321SS (right).

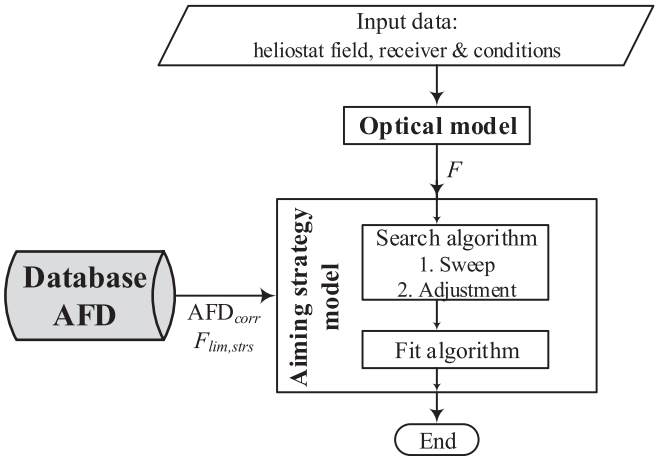

Fig. 10. Flowchart with inputs to the aiming strategy model.

actually found in the intersection between $F_{lim,strs}$ and the actual incident flux distribution F, as will be shown in next Section with the aid of Fig. 13.

4. Heliostat field aiming strategy

The methodology to generate databases of allowable flux densities has been described in the previous sections, providing examples for different tube alloys and geometries. This way, corrosion (Section 2) and thermal stress (Section 3) constraints have been translated into AFD, which can be handled by optical models and, specifically, the heliostat field aiming strategy.

The goal of the aiming strategy model is to point each and every heliostat in the field in such a way that the receiver thermal output (*i.e.* receiver interception) is maximized, while corrosion and thermal stress constraints are met at the same time. This model, described in detail in Ref. [5], consists of two sequential algorithms named *Search* and *Fit*. In the end, the aiming model adjusts the real flux density profiles from the heliostat field to the AFD limit gathered from the database.

Fig. 10 represents the flowchart of data in the aiming strategy, where the database of AFD provides the necessary (and valuable) input to the model. Solar flux density on the receiver is calculated with **FluxSPT** software tool [17,18].

To illustrate the output of the aiming strategy model using the generated databases of AFD, it is taken Gemasolar SPT plant, located in Fuentes de Andalucía, Spain, at 37.56° north latitude. The surrounding heliostat field consists of 2650 square heliostats of 115.7 m^2 reflective surface [19]. Fig. 11 shows the layout of Gemasolar field, where rows are colored for proper identification of heliostats in the aiming maps.

Gemasolar receiver, located atop of a 120 m high tower, comprises 18 panels arranged around a cylindrical shell of 8.5 m in diameter and 10.5 m in height. Even though AFD databases for several tube geometries were generated previously, this Section considers credible tubes of 25 mm in outer diameter and 1.5 mm wall thickness. Therefore, each panel comprises 57 tubes, assuming 1 mm of separation between tubes. Serpentine flow pattern throughout the panels is considered, starting from the north where total flow is divided in two flowpaths (east and west, 9 panels each). Receiver geometry and flow pattern are displayed in Fig. 12, along with the 43 aim levels herein considered.

The aiming strategy model firstly runs the single aiming case (all heliostat aim to the equatorial aim level), from which the preliminary AFD limits by corrosion and thermal stress are set. Once $\dot{m}_{s,t}$ and T_s are known, AFD_{corr} is unequivocally determined. And similarly, $F_{lim,strs}$ is decided by T_s and T_w.

For summer solstice at 10 h solar time, Fig. 13 represents the profiles of flux density (black solid line) and the AFD both by corrosion (orange) and thermal stress (magenta) for Inconel 625 tubes. The ultimate AFD limit is definitely the minimum between AFD_{corr} and AFD_{strs} along the receiver; east and west flowpaths are respectively displayed in left and right sides of the figure. Where F exceeds AFD_{corr} or AFD_{strs}, the corresponding requirement (either corrosion or thermal stress) is not met. At the bottom of Fig. 13, where the profiles of salt and film temperature are outlined, it can be checked in the last panels that flux densities over the AFD_{corr} limit incurs in film temperatures also above the 628 °C limit for In625.

Similarly, F values over $F_{lim,strs}$ blue line (top of Fig. 13) implies thermal stresses higher than the *UTS* of In625. As previously pointed out,

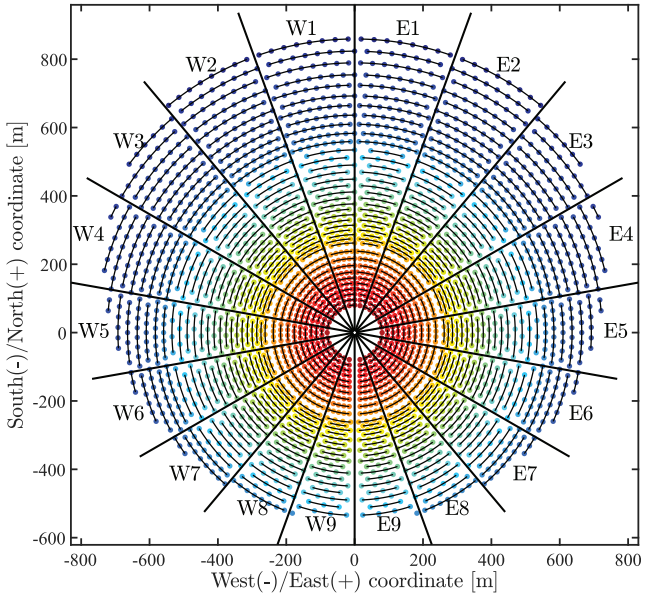

Fig. 11. Layout of Gemasolar heliostat field.

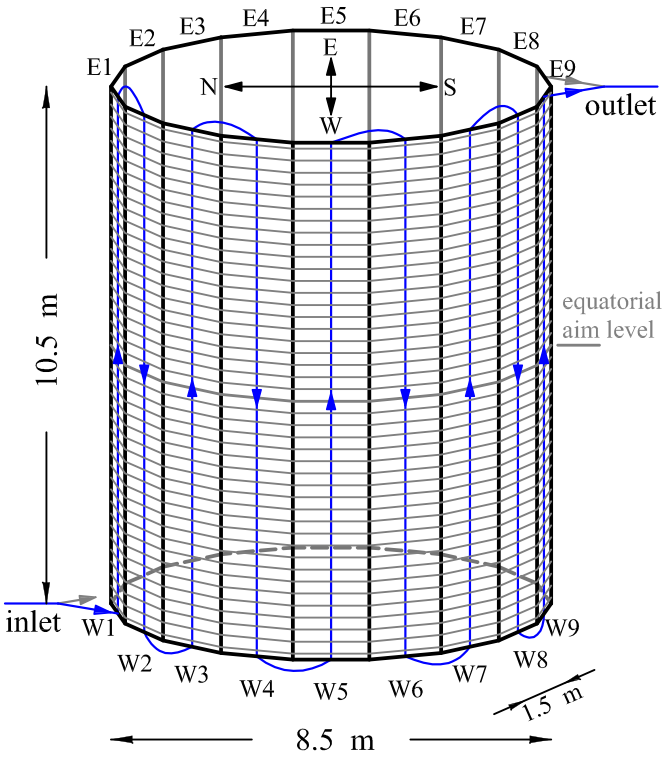

Fig. 12. Receiver geometry, flowpaths and aim levels.

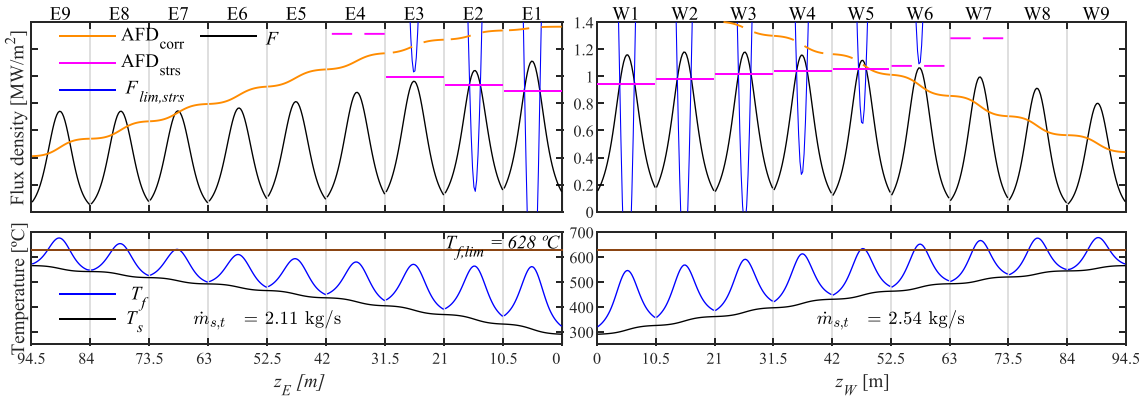

Fig. 13. Profiles of flux density (top) and temperatures (bottom) for In625 tubes ($d_o = 25mm$, $t = 1.5mm$). Equatorial aiming at 10 h summer solstice noon.

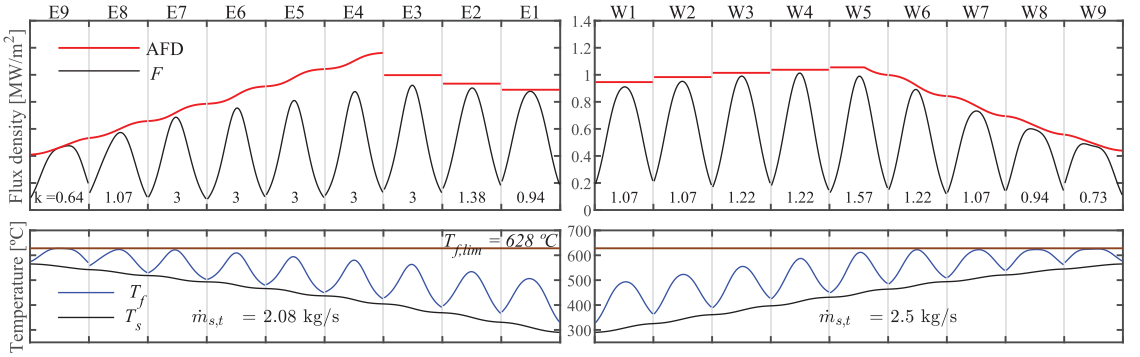

(a) Inconel 625

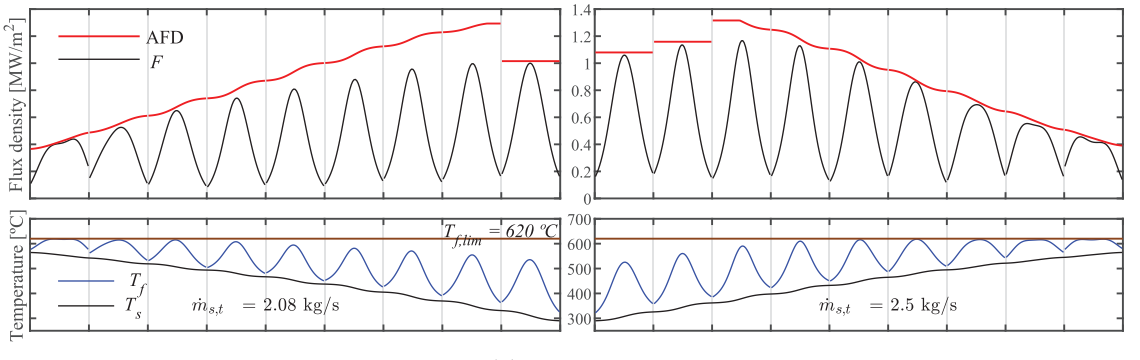

(b) Haynes 230

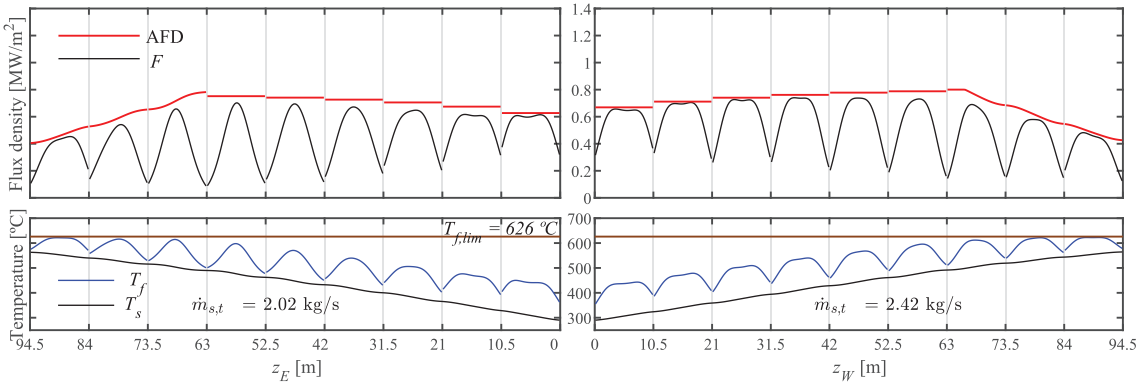

(c) 321SS

Fig. 14. Optimized aiming at 10 h summer solstice noon. Profiles of flux density (top) and temperatures (bottom) for tubes of: (a) In625, (b) HA230, and (c) 321SS. ($d_o = 25mm$, $t = 1.5mm$).

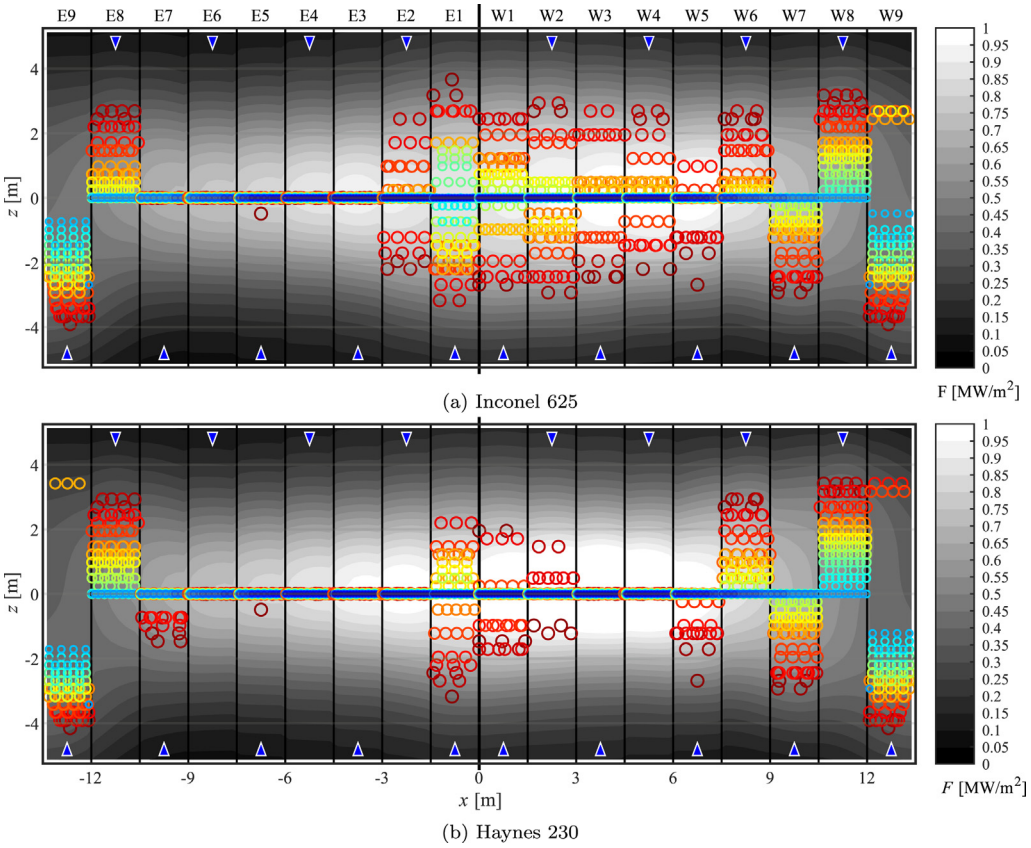

Fig. 15. Flux and aiming map at 10 h summer solstice for tubes of: (a) In625, and (b) HA230. ($d_o = 25mm$, $t = 1.5mm$).

the allowable flux density by thermal stress is indeed in the intersection between F and $F_{lim,strs}$, which is marked in the figure by the AFD_{strs} magenta horizontal segments.

Starting from the equatorial aiming (as in Fig. 13), the aiming strategy model computes the aiming of the heliostats in the field so that the resulting flux density profile F is below –or matches– the AFD limit. Such limit is actually updated from the AFD database during algorithms calculation, accounting for the interaction between changing field aiming and receiver thermal performance. The aiming algorithms grounds in the control of a single parameter, named k aiming factor. Extensive details on this parameter can be found in Ref. [18].

The AFD databases, described and generated in this paper, feed the aiming strategy model leading to results like the following. Again for summer solstice at 10 h, Fig. 14 represents the final flux and temperature profiles for In625 (a), HA230 (b), and 321SS (c). As required, flux profiles do not surpass the AFD limits.

From Fig. 14 it is concluded that receiver tubes of HA230 result in less thermal stress limitation than In625; roughly speaking, three panels and a half *vs.* seven and a half are respectively affected (flat red limit). For 321SS, thermal stress constraint is more stringent yet; most of the panels are affected and the AFD_{strs} is very low, around 700 kW/m^2. This is consistent with the behavior shown from the $F_{lim,strs}$ databases presented in Section 3.

While the first (northern) panels are restricted by thermal stress, corrosion becomes limiting in the last (southern) panels; where salt temperature is higher. It is in these panels where the necessity of proper heliostat aiming is usually more relevant, as can be interpreted from the fitting between the profiles of F and AFD.

Despite HA230 has better mechanical performance than In625, and since the corrosion film temperature is smaller in the former alloy, the final thermal output turns out almost the same in both cases. As can be examined from table 2, the thermal power absorbed by molten-salt is 109.1 MW with In625, and 108.9 MW with HA230.

The following figure shows two examples of the final output from the aiming model for receivers made of Inconel 625 (Fig. 15a) and Haynes 230 (Fig. 15b). These figures represent both the resulting –optimal– flux map (grayscale background) and the aiming map, where the circles mark the aiming point of each heliostat in the field. The jet colormap for the aim points assigns hot colors to the near heliostats and cold colors to the far ones. Precise correspondence can be established with the Gemasolar

Table 2
Receiver thermal output and spillage factor along summer solstice for selected alloys. ($d_o = 25mm$, $t = 1.5mm$).

Solar time		12	11	10	9	8	7	6
DNI [W/m^2]		930	930	920	910	860	770	600
Q_{rec} [MW]	In625	114.3	113.4	109.1	102.8	90.7	72.5	43.3
	HA230	114.3	113.2	108.9	102.4	90.5	72.2	43.2
	321SS	110.2	109.6	105.7	100.2	89.0	71.5	43.3
	347SS	107.9	107.3	103.4	98.1	87.5	71.0	43.4
f_{sp} [%]	In625	81.0	81.0	80.9	80.6	80.2	79.7	79.1
	HA230	80.9	80.8	80.7	80.3	80.0	79.4	78.9
	321SS	78.7	78.9	78.9	79.0	79.0	78.8	79.1
	347SS	77.3	77.4	77.4	77.6	77.9	78.3	79.2

colored layout, previously shown in Fig. 11.

For the In625 receiver, Fig. 15a reveals that the central panels in the east side of the receiver are targeted to its equator by the corresponding heliostats. This result can be also deduced from the $k = 3$ aiming factor shown in Fig. 14a. In contrast, a wide spreading of the aim points is required in the rest of the panels to maintain the structural integrity of the receiver.

For the same instant of time, the aiming strategy for HA230 receiver is lightly less demanding (Fig. 15b). Lower spread of the aiming points is required, so that even panels 3 and 4 in the west flowpath allow for equatorial aiming.

Table 2 summarizes the resulting receiver power output (Q_{rec}) throughout summer solstice for the four selected alloys. Nickel-based alloys achieve better performance, in contrast to austenitic alloys; especially in the central hours of the day. HA230 and In625 yield similar results. The slightly higher corrosion tolerance of In625 compensates the better mechanical performance of HA230.

The same conclusion is yielded by having a look to the resulting spillage loss factors (f_{sp}) in the bottom part of Table 2. The spillage factor accounts for the concentrated radiation from the heliostat field actually intercepted by the receiver. As no spillage represents $f_{sp} = 1$, the higher f_{sp} is, the better the aiming performance is.

5. Conclusions

Corrosion and thermal stress limitations in molten-salt receivers have been translated into Allowable Flux Densities (AFD), using the methodologies described in the present paper. The influence of tube material and geometry have been examined.

On the basis of experimental data, molten-salt temperature limits for corrosion have been determined for selected alloys, being 628 and 620 °C respectively for In625 and HA230. A thermal model has been used to determine the incident flux producing such limiting film temperature, this way generating the database of AFD_{corr} that depends on salt mass flow rate and bulk temperature. AFD_{corr} increases with growing $\dot{m}_{s,t}$, but decreases with growing T_s. The thickness increment of the tube wall lowers slightly the AFD_{corr}.

An expression of $F_{lim,strs}$, limiting flux density by thermal stress, has been obtained by combining equations from heat transfer and Babcock & Wilcox stress [12] in irradiated tubes. $F_{lim,strs}$ increases with growing T_s, but decreases with growing T_w. Thicker wall tubes have a disastrous effect on $F_{lim,strs}$. In the intersection between such flux limit, and actual incident flux is found the AFDS.

Finally, the generated AFD databases have been used to feed the aiming strategy model, applied to Gemasolar case study. The final goal of the aiming strategy is to maximize the receiver output, while meeting corrosion and thermal stress below the limit [5]. This AFD-based approach saves extensive computation time to the aiming model, that straightforwardly works in terms of flux density rather than film temperatures or mechanical stresses.

The first panels of the cylindrical receiver are restricted by thermal stress, whilst corrosion constricts the last ones. Receiver of nickel-based alloy tubes perform better than that of austenitic ones. Even though HA230 has better mechanical performance than In625, receiver thermal output under the optimized aiming is almost the same for both alloys; which is explained by the slightly higher tolerance to corrosion of In625. Even though it is beyond the scope of the present study, creep-fatigue behavior of both HA230 and In625 should be also researched.

Author contribution statement

Alberto Sánchez-González: Conceptualization, Methodology, Software, Validation, Writing – Original Draft, Visualization. **María Reyes Rodríguez-Sánchez:** Software, Writing – Review & Editing, Funding acquisition. **Domingo Santana:** Writing – Review & Editing, Supervision.

Declaration of competing interest

The authors declare that there is no conflict of interest.

Acknowledgments

This study has been supported and financed by Iberdrola España Foundation under the program *Ayudas a la investigación en Energía y Medio Ambiente 2018*, project: "Diseño y evaluación de un Nuevo receptor solar exterior de tubos ovalados". The authors acknowledge to 11CNIT (XI National and II International Engineering Thermodynamics Congress) committee for selecting the previous conference contribution for further dissemination through this special issue.

References

[1] J.W. Slusser, J.B. Titcomb, M.T. Heffelfinger, B.R. Dunbobbin, Corrosion in molten nitrate-nitrite salts, J. Occup. Med. 37 (7) (1985) 24–27, doi:10.1007/BF03259692, http://link.springer.com/10.1007/BF03259692.

[2] L.L. Vant-Hull, The role of "allowable flux density" in the design and operation of molten-salt solar central receivers, J. Sol. Energy Eng. 124 (2) (2002) 165, doi:10.1115/1.1464124, http://solarenergyengineering.asmedigitalcollection.asme.org/article.aspx?articleid=1456457.

[3] Z. Liao, X. Li, C. Xu, C. Chang, Z. Wang, Allowable flux density on a solar central receiver, Renew. Energy 62 (2014) 747–753, doi:10.1016/j.renene.2013.08.044, http://linkinghub.elsevier.com/retrieve/pii/S0960148113004606.

[4] Y. Luo, X. Du, L. Yang, C. Xu, Y. Yang, Study on the allowable flux density for a solar central dual-receiver, in: SolarPACES, vol. 69, 2014, pp. 138–147, doi:10.1016/j.egypro.2015.03.017, http://linkinghub.elsevier.com/retrieve/pii/S1876610215003239.

[5] A. Sánchez-González, M.R. Rodríguez-Sánchez, D. Santana, Aiming strategy model based on allowable flux densities for molten salt central receivers, Sol. Energy 157 (2017) 1130–1144, doi:10.1016/j.solener.2015.12.055, http://linkinghub.elsevier.com/retrieve/pii/S0038092X16001468.

[6] R. Flesch, C. Frantz, D. Maldonado Quinto, P. Schwarzbözl, Towards an optimal aiming for molten salt power towers, Sol. Energy 155 (2017) 1273–1281, https://doi.org/10.1016/j.solener.2017.07.067, doi:10.1016/j.solener.2017.07.067.

[7] J. García, Y.C. Soo Too, R.V. Padilla, A. Beath, J.-S. Kim, M.E. Sanjuan, Dynamic performance of an aiming control methodology for solar central receivers due to cloud disturbances, Renew. Energy 121 (2018) 355–367, doi:10.1016/j.renene.2018.01.019, http://linkinghub.elsevier.com/retrieve/pii/S0960148118300193.

[8] A.M. Kruizenga, D.D. Gill, M. Laford, G. McConohy, Corrosion of High Temperature Alloys in Solar Salt at 400, 500, and 680 C, 2013. Tech. rep., SAND 2013-8256.

[9] M. Rodríguez-Sánchez, A. Soria-Verdugo, J.A. Almendros-Ibáñez, A. Acosta-Iborra, D. Santana, Thermal design guidelines of solar power towers, Appl. Therm. Eng. 63 (1) (2014) 428–438, doi:10.1016/j.applthermaleng.2013.11.014, http://www.sciencedirect.com/science/article/pii/S1359431113008028.

[10] M.F. Modest, Radiative Heat Transfer, second ed., Academic press, Amsterdam, 2003.

[11] A.B. Zavoico, Solar Power Tower: Design Basis Document, Tech. Rep. July, Sandia National Laboratories, 2001. SAND2001-2100.

[12] Babcock & Wilcox, Molten Salt Receiver Subsystem Research Experiment, Phase I - Final Report, Tech. Rep. SAND82-8178, Tech. rep., 1984 https://ntrl.ntis.gov/NTRL/dashboard/searchResults/titleDetail/DE85002669.xhtml.

[13] W.R. Logie, J.D. Pye, J. Coventry, Thermoelastic stress in concentrating solar receiver tubes: a retrospect on stress analysis methodology, and comparison of salt and sodium, Sol. Energy 160 (November 2017) (2018) 368–379, doi:10.1016/j.solener.2017.12.003, http://linkinghub.elsevier.com/retrieve/pii/S0038092X17310757.

[14] M.R. Rodríguez-Sánchez, C. Marugán-Cruz, A. Acosta-Iborra, D. Santana, Thermo-mechanical modelling of solar central receivers: effect of incident solar flux resolution, Sol. Energy 165 (February) (2018) 43–54, https://doi.org/10.1016/j.solener.2018.03.005.

[15] American society of mechanical engineering, section II materials, Part D: properties, in: ASME Boiler and Pressure Vessel Code, 2010.

[16] D.L. Siebers, J.S. Kraabel, Estimating Convective Energy Losses from Solar Central Receivers, Tech. rep., Sandia National Laboratories, 1984. SAND84-8717

[17] A. Sánchez-González, D. Santana, Solar flux distribution on central receivers: a projection method from analytic function, Renew. Energy 74 (2015) 576–587, doi:10.1016/j.renene.2014.08.016, http://linkinghub.elsevier.com/retrieve/pii/S0960148114004753.

[18] A. Sánchez-González, M.R. Rodríguez-Sánchez, D. Santana, Aiming factor to flatten the flux distribution on cylindrical receivers, Energy 153 (2018) 113–125, doi:10.1016/j.energy.2018.04.002, http://linkinghub.elsevier.com/retrieve/pii/S0360544218305929.

[19] J.M. Lata, S. Alcalde, D. Fernández, X. Lekube, First surrounding field of heliostats in the world for commercial solar power plants - Gemasolar, in: Proceedings of SolarPACES, 2010.